Updates on the Radar Data Quality Control in the MRMS Quantitative Precipitation Estimation System

LIN TANG,[a] JIAN ZHANG,[b] MICHEAL SIMPSON,[a] AMI ARTHUR,[a] HEATHER GRAMS,[c] YADONG WANG,[d] AND CARRIE LANGSTON[a]

[a] *Cooperative Institute for Mesoscale Meteorological Studies, University of Oklahoma, Norman, Oklahoma*
[b] *NOAA/OAR/National Severe Storms Laboratory, Norman, Oklahoma*
[c] *NOAA/NWS/Radar Operations Center, Norman, Oklahoma*
[d] *Electrical and Computer Engineering, Southern Illinois University Edwardsville, Edwardsville, Illinois*

(Manuscript received 30 September 2019, in final form 24 May 2020)

ABSTRACT

The Multi-Radar-Multi-Sensor (MRMS) system was transitioned into operations at the National Centers for Environmental Prediction in the fall of 2014. It provides high-quality and high-resolution severe weather and precipitation products for meteorology, hydrology, and aviation applications. Among processing modules, the radar data quality control (QC) plays a critical role in effectively identifying and removing various nonhydrometeor radar echoes for accurate quantitative precipitation estimation (QPE). Since its initial implementation in 2014, the radar QC has undergone continuous refinements and enhancements to ensure its robust performance across seasons and all regions in the continental United States and southern Canada. These updates include 1) improved melting-layer delineation, 2) clearance of wind farm contamination, 3) mitigation of corrupt data impacts due to hardware issues, 4) mitigation of sun spikes, and 5) mitigation of residual ground/lake/sea clutter due to sidelobe effects and anomalous propagation. This paper provides an overview of the MRMS radar data QC enhancements since 2014.

1. Introduction

The Multi-Radar Multi-Sensor (MRMS) system (Zhang et al. 2016; Smith et al. 2016) integrates data from multiple radars, rain gauges, lightning detection systems, and forecast models, and delivers a suite of severe weather and quantitative precipitation estimation (QPE) products for severe weather, flash flood, and river flood forecasts and warnings. Among various input data sources, radar observations have a high spatial and temporal resolution, providing three-dimensional coverage of weather systems. As a result, radar data are essential and crucial for the MRMS product generation. The radar data quality control (QC) plays a critical role in assuring high-quality MRMS products. MRMS radar data QC contains two major components: the dual-polarization radar QC developed by Tang et al. (2014) (hereafter ''dpQC''), and the single-polarization radar QC developed by Zhang et al. (2004) and Lakshmanan et al. (2012). The former was applied to the U.S. Weather Surveillance Radar-1988 Doppler (WSR-88D) network (S-band dual polarization) while the latter to the Environment Canadian radar network (C-band single polarization).

In weather studies, the nonmeteorological radar echoes include biological clutter (i.e., birds and insects), the electromagnetic interference with transmitters (e.g., sun strobes), the ground/sea clutter, anomalous propagation, and the echoes from the chaff or other nonweather targets. There are different discrimination algorithms to separate nonprecipitation echoes from the weather information (Berenguer et al. 2006; Gourley et al. 2007; Lakshmanan et al. 2014; Chandrasekar et al. 2013; Krause 2016) and to classify different hydrometeors further using the dual-polarization radar data (Liu and Chandrasekar 2000; Park et al. 2009). Due to its simplicity and effectiveness, the dpQC has been applied in the MRMS system since 2014. It is based on the distinctly different characteristics of correlation coefficient (ρ_{HV}) for hydrometeor and nonhydrometeor returns (Balakrishnan and Zrnić 1990; Doviak and Zrnić 1993; Zrnić and Ryzhkov 1999; Berenguer et al. 2006; Melnikov and Zrnić 2007; Kumjian 2013a). The dpQC combines ρ_{HV} filters that separate precipitation (high ρ_{HV} values)

Corresponding author: Lin Tang, lin.tang@noaa.gov

DOI: 10.1175/JTECH-D-19-0165.1

from nonprecipitation (low ρ_{HV} values) areas with a set of heuristic rules that handle exceptions to the basic ρ_{HV} filters. Such exceptions include 1) areas of hail, nonuniform beam filling, and a melting layer (ML) associated with low ρ_{HV} values, and 2) clutter and biological pixels with high ρ_{HV} values. Zhang et al. (2004) used intensity, texture, and vertical continuity of reflectivity (Z) to identify ground clutter and biological returns from normal and anomalous propagations (AP). Lakshmanan et al. (2012) developed a statistical approach to creating seasonal clutter maps for each radar. The statistical clutter removal was necessary for reducing the contaminations from ground clutter because the clutter mitigation in signal processing was limited in Canadian radars. It is worth noting that the Canadian radar network is undergoing an upgrade to S-band polarimetric capabilities. The dpQC application would significantly improve the data quality once the upgrade is complete.

This work is to refine and improve the QC algorithms in the MRMS system based on real-time observations and operational feedback. Such issues include but are not limited to erroneous removal of mixed-phase precipitation due to inaccurate background freezing-level information, residual clutter of sun spikes, and wind farms (WF). Further, a hardware issue was identified recently, causing corruption in dual-polarization radar fields and sometimes a wipeout of the entire radar domain. For Canadian radars, the sea or lake clutter was found from a few radars located near the Lake Superior and the Gulf of St. Lawrence. Several refinements were made to the radar QC algorithms in MRMS to address these issues. Those improvements include 1) melting-layer delineation, 2) clearance of wind farm contamination, 3) mitigation of corrupt data impacts due to hardware issues, 4) mitigation of residual clutter and sun spikes, and 5) reduction of residual ground/river/lake clutter due to sidelobe effects and AP. This paper provides an overview of these refinements and their impacts on the MRMS products.

The paper is organized as follows. Section 2 provides the details of the improvements through case studies. Section 3 presents the performance of the updated QC algorithm and evaluations through real-time observations. A summary and future work are given in section 4.

2. Overview of MRMS radar QC updates

a. Reduced false alarms in the melting hydrometeors

The ML consists of melting snow aggregates (stratiform precipitation) or melting graupel or hail (convective precipitation; Brandes and Ikeda 2004). The ML depth is generally a few hundred meters near the 0°C height based on profiler radar observations (Fabry and Zawadzki 1995). Due to the beam broadening effect, the ML may impact WSR-88D measurements for a much thicker layer, especially on a low elevation angle (e.g., Zhang and Qi 2010; Andrić et al. 2013).

When radar beams propagate through the ML, radar variables of Z (ρ_{HV}) generally show increased (decreased) values (Brandes and Ikeda 2004; Kumjian 2013b). The low ρ_{HV} feature caused by melting hydrometeors shows a similar signature as those caused by nonprecipitation clutter. ML detection algorithms using different combinations of polarimetric radar variables have been developed during the past two decades (e.g., White et al. 2002; Gourley and Calvert 2003; Tabary et al. 2006; Giangrande et al. 2008; Wolfensberger et al. 2016). The dpQC utilizes the combination of ρ_{HV} features and the temperature profile to delineate the bottom of the melting layer (Tang et al. 2014). The algorithm catches the ''belt'' shape of ρ_{HV} (observed in the plan position indicator) near the 0°C height, where the average ρ_{HV} decreases among the melting zone and stays high in the below/above regions. The actual ML thickness and contour is adjusted using the ρ_{HV} field.

Using a single 0°C height as reference causes issues in the dpQC when temperature horizontal gradients are large, e.g., near frontal zones. Figure 1 demonstrates an example using the data collected from the radar at La Crosse, Wisconsin (KARX), at 0003 UTC 14 April 2014. The sounding at the radar site showed a 0°C height of 1.1 km above the mean sea level. With the input of single reference height as the reference, the dpQC only delineated a small region to the northwest of the radar (white area, Fig. 1a) as a potential ML region, but did not catch the ''belt'' ρ_{HV} feature in other directions because of the high elevation in the 0°C height. As a result, some precipitation echoes with relatively low ρ_{HV} (black rectangle, Fig. 1b) were removed incorrectly (black rectangle, Fig. 1c). The single freezing-level reference height used in Tang et al. (2014) was replaced with a two-dimensional freezing-level height field in the updated dpQC (''dpQC2'' hereafter), which provides more accurate delineation reference ML heights across the radar domain.

The two-dimensional freezing-level field was derived from a combination of the contiguous U.S. (CONUS) High-Resolution Rapid Refresh (HRRR) and the Rapid Refresh (RAP) (Benjamin et al. 2009, 2011, 2013, 2016) model analyses to encompass the MRMS domain. The hourly updated HRRR and RAP models

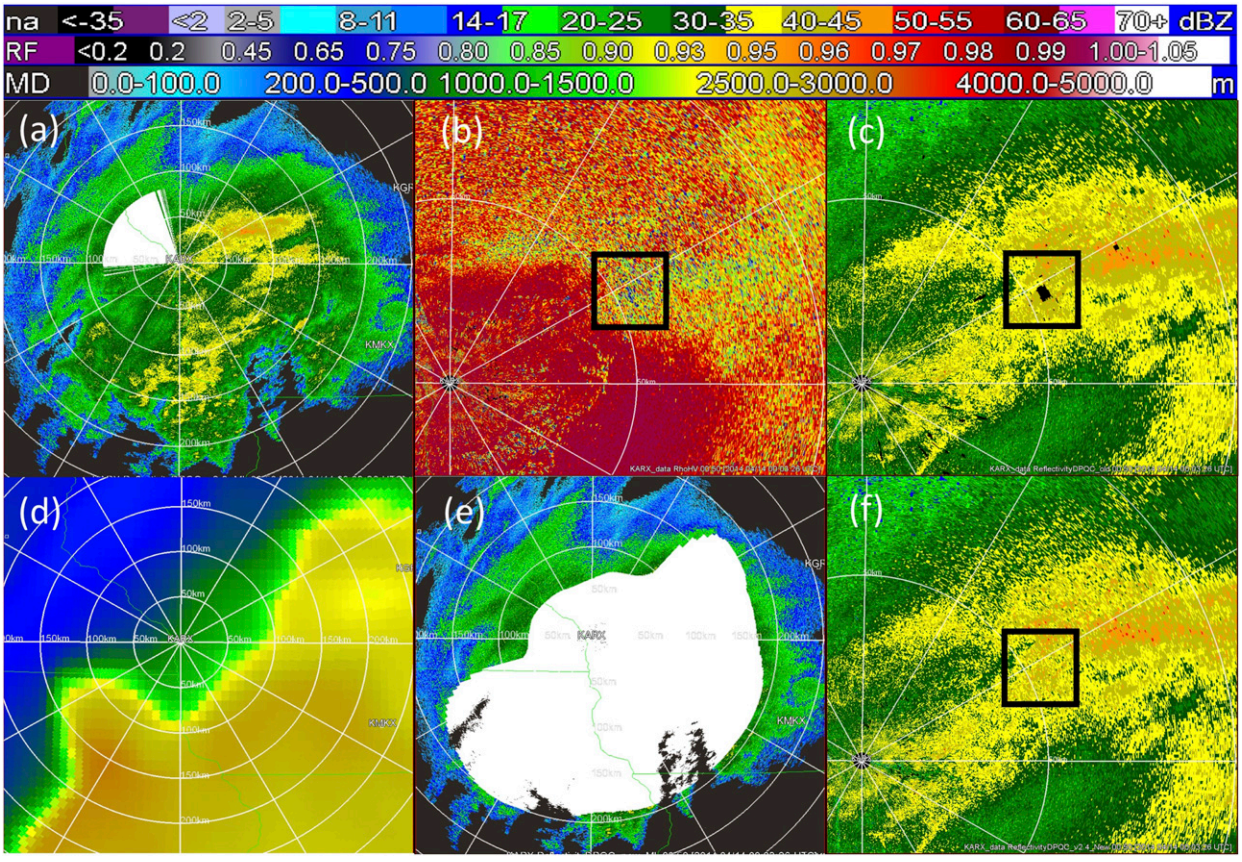

FIG. 1. An example case to show the changes using different model data inputs to the radar at La Crosse (KARX). With the information of single model sounding data, the dpQC delineated a small region of ML, which was highlighted in white on top of the Z field observation in (a). (b) The zoom-in ρ_{HV} field and (c) the QCed Z field with false alarms. (d) The two-dimensional field of 0°C height close to radar KARX derived from the CONUS HRRR and RAP. (e) The ML area identified using the two-dimensional model data. (f) The Z field processed with the updated dpQC2. The rectangle frame highlights the region of melting hydrometeor that is mistakenly removed in (c). These precipitation echoes are retained in the updated scheme in (f). The model data are valid at the 0000 UTC, and the radar data are observed at 0003 UTC 14 Apr 2014.

have 3- and 13-km resolutions, respectively. Figure 1d shows the strong horizontal gradient across the radar. The two-dimensional model analysis indicated a freezing level ranging from 0.5 km (northwest) to 3.2 km (southeast) above the mean sea level within a distance of 100 km.

In dpQC2, the melting likelihood field (S) (e.g., Fig. 2b) is created as follows:

$$\text{If}\begin{cases} 0.80 \le \rho_{HV}(i,j) < 0.98 \\ 0.98 \le \rho_{HV}(i,j) \le 1.00 \\ \rho_{HV}(i,j) > 1.00 \\ \rho_{HV}(i,j) < 0.80 \\ \rho_{HV}(i,j) = \text{missing} \end{cases} \text{then} \begin{cases} S(i,j) = 3 & \text{Possible melting particles} \\ S(i,j) = 2 & \text{Liquid precipitation} \\ S(i,j) = 1 & \text{Low SNR weak echoes} \\ S(i,j) = 0 & \text{Nonprecipitation} \\ S(i,j) = -1 & \text{Missing echoes} \end{cases}, \quad (1)$$

where i and j are the indices along azimuth and range directions, respectively. The melting likelihood field is an initial grouping based on ρ_{HV} ranges from different scatterers (Kumjian 2013a). At the operating frequency of WSR-88Ds (S band), pure rain produces high values of ρ_{HV} (>0.98), and the nonmeteorological scatterers generally yield low ρ_{HV} (<0.80). Three zones near the 0°C height (e.g., Fig. 2a) are defined as ML^-, ML^0, and ML^+ as follows:

$$\begin{cases} H_{0°C_L} - 2\,\text{km} \le h(r) < H_{0°C_L} - 1\,\text{km} & ML^- \\ H_{0°C_L} - 1\,\text{km} \le h(r) < H_{0°C_H} & ML^0 \\ H_{0°C_H} \le h(r) < H_{0°C_H} + 1\,\text{km} & ML^+ \end{cases}, \quad (2.1)$$

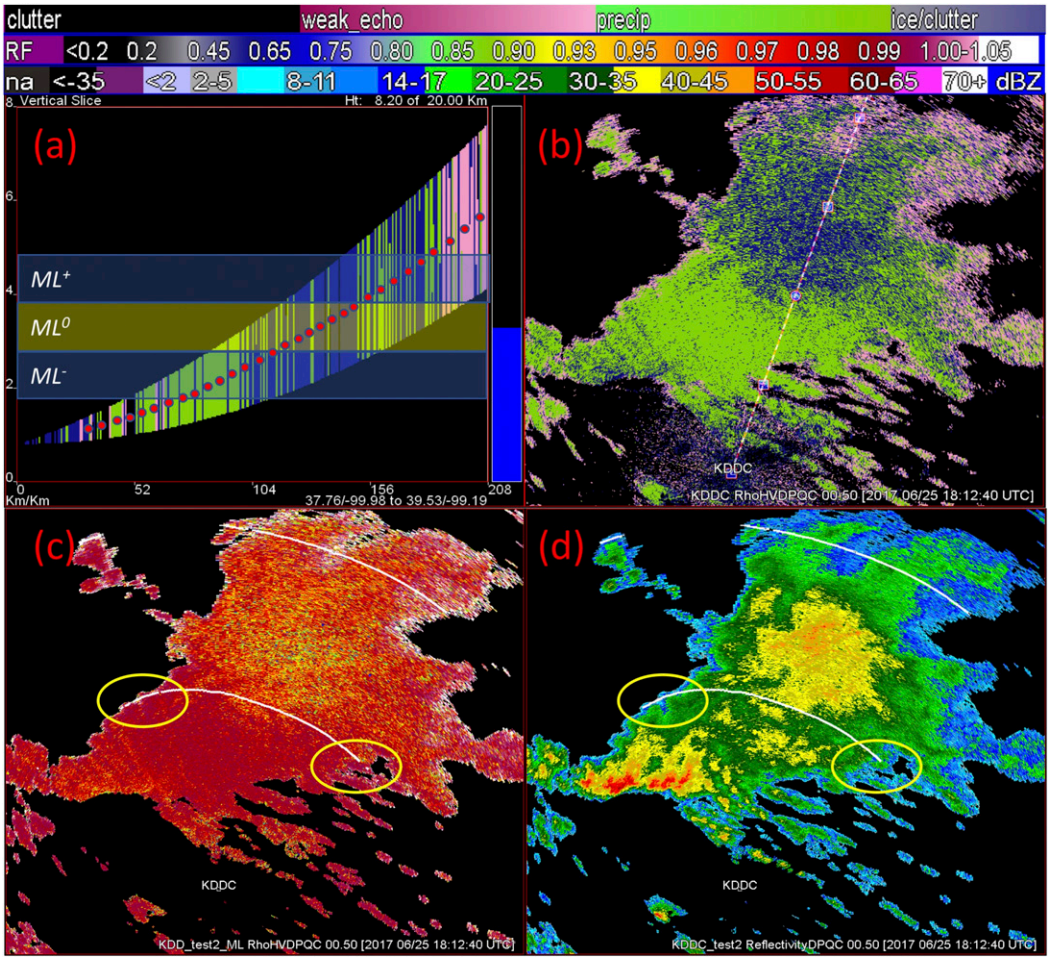

FIG. 2. (a) The range–height indicator (RHI) and (b) the plan position indicator (PPI) of the melting likely (S) field. (c) The melting-layer outlines (white lines) on top of the ρ_{HV} and (d) the outlines on top of the Z field after the quality control. All fields validate at 1812 UTC 25 Aug 2017, observed by radar KDDC at Dodge City. In (a) the RHI of the radar beam is shown at 0.5° elevation along the direction marked in (b). The red dots pinpoint the radar beam center, and the three sections in Eq. (2.2) are indicated as transparent blue–yellow–blue zones. The yellow ellipses in (c) and (d) highlight the difference before and after the outline smoothing.

$$\begin{cases} H_{0^\circ C_M} - 2\,\text{km} \le h(r) < H_{0^\circ C_M} - 1\,\text{km} & \text{ML}^- \\ H_{0^\circ C_M} - 1\,\text{km} \le h(r) < H_{0^\circ C_M} & \text{ML}^0 \\ H_{0^\circ C_M} \le h(r) < H_{0^\circ C_M} + 1\,\text{km} & \text{ML}^+ \end{cases}, \tag{2.2}$$

where $h(r)$ is the radar beam (center) height at the bin of range r. Based on the two-dimensional 0°C height (e.g., Fig. 1d), the radar data at each bin are associated with one referential 0°C height correspondingly. The terms$H_{0^\circ C_L}$ and $H_{0^\circ C_H}$ are the lowest and highest 0°C heights along this radial direction, respectively; $H_{0^\circ C_M}$ is the average 0°C heights. Equations (2.1) and (2.2) are applied when the difference between $H_{0^\circ C_L}$ and $H_{0^\circ C_H}$ is larger and less than 1 km, respectively. Figure 2 shows example fields from the radar at Dodge City (KDDC). Figure 2a is the range–height indicator of the S field at 0.5° elevation along the direction marked in Fig. 2b. The red dots pinpoint the radar beam center, and the transparent blue–yellow–blue zones indicate the three sections in Eq. (2.2). The average S in these three zones [Eqs. (3.1)–(3.3)] and ρ_{HV} in ML^0 [Eq. (3.4)] are then calculated for each radial:

$$S^- = \begin{cases} \dfrac{1}{N^-}\sum_1^{N^-} S(r) & N^- > 0 \\ 0 & N^- = 0 \end{cases}, \quad \text{ML}^-, \tag{3.1}$$

$$S^0 = \begin{cases} \dfrac{1}{N^0}\sum_1^{N^0} S(r) & N^0 > 0 \\ 0 & N^0 = 0 \end{cases}, \quad \text{ML}^0, \tag{3.2}$$

$$S^{+} = \begin{cases} \dfrac{1}{N^{+}} \sum_{1}^{N^{+}} S(r) & N^{+} > 0 \\ 0 & N^{+} = 0 \end{cases}, \quad \mathrm{ML}^{+}, \tag{3.3}$$

$$\rho_{\mathrm{HV}}^{0} = \begin{cases} \dfrac{1}{N^{0}} \sum_{1}^{N^{0}} \rho_{\mathrm{HV}}^{0}(r) & N^{0} > 0 \\ 0 & N^{0} = 0 \end{cases}, \quad \mathrm{ML}^{0}, \tag{3.4}$$

where N^{+}, N^{0}, and N^{-} are the total gate numbers of possible melting particles, liquid precipitation, and nonprecipitation [Eq. (1)] in each of the three zones, respectively. Derived from Eqs. (3.1)–(3.4), if the average ρ_{HV}^{0} is larger than 0.90 and the average melting likelihood S^{0} in ML^{0} is larger than the S^{-} and S^{+} from the other two layers, the radial potentially contains a melting region. The pixels inside the melting area are retained as precipitation echoes regardless of their ρ_{HV} values. Although the majority of precipitation echoes have a ρ_{HV} between 0.80 and 0.98, the melting hydrometeors could be associated with lower values (<0.80). This process is performed radially for the entire volume data. As indicated in Fig. 2c, the recorded ML top/bottom heights are marked with white lines on the top of the ρ_{HV} field. The white lines are smoothed in the azimuthal direction to keep the spatial continuity (Fig. 2d). In the example of radar KARX, Fig. 1e shows the potential ML areas derived from the two-dimensional reference freezing level, and Fig. 1a is the result using a single reference 0°C height. The dpQC2 preserves the precipitation echoes associated with low ρ_{HV} (black rectangle, Fig. 1f).

Note that the ML region does not label melting hydrometeors pixel by pixel but instead provides an approximate range potentially impacted by the ML. The new ML delineation reduces the erroneous removal of mixed-phase hydrometeors.

b. Clearance of the wind farm contamination

As an ideal environmental clean power resource, the wind energy industry has grown significantly in the United States since the 1970s. However, large-size wind turbines, together with the rotation of the blades, cause interference in the radar echoes observed by weather radar systems (Isom et al. 2009; Vogt et al. 2007; Norin and Haase 2012). The established wind farms located in the WSR-88D beam of sight show that wind turbine clutter impacts the radar measurement as well as an internal algorithm that generates alerts and derived weather products, such as precipitation estimation (Vogt et al. 2011).

To identify the location of a wind turbine and mitigate its interferences on radar echoes, automatic wind turbine detection algorithms have been developed using single- or dual-polarization radars. For example, Hood et al. (2010) proposed a fuzzy-logic based detection approach, which integrates variables derived from level-I time series data such as spectral flatness, higher-order spectral moment, clutter phase alignment, and hub-to-weather ratio. A similar fuzzy logic approach using level-II single-polarization data (Z, radial velocity V_r, and spectrum width σ_v) was developed by Cheong et al. (2011). Other signal processing techniques include the work from Bachmann et al. (2010), Nai et al. (2011), etc., and these adaptive clutter filters require level-I raw data as inputs. With the dual-polarization capability, the low ρ_{HV} signature is used as an indicator of wind turbine clutter. However, cases are observed where low ρ_{HV} caused by wind turbines is not distinct from weather signals. For example, the hydrometeors mixed in size and shape (i.e., big drops, hail) could also be associated with the low ρ_{HV}. It is challenging when the power returns from WF are embedded in convective storms. Although the WF clutter residue is only observed sometimes, the accumulated QPE could be biased from even a few scans. This refinement of the QC process on WFs can remove the contamination from wind turbines.

1) WF IDENTIFICATION

An efficient and robust method to identify areas from wind turbine clutter is to generate a lookup table of wind turbine location. The first version of the table, including wind turbine locations and their effect areas (wind turbine clutter), was generated by National Severe Storms Laboratory (NSSL) in 2010. To ensure the most accurate and updated dataset of wind turbine locations, numerous sources of information were compiled and cross-referenced with each other since the first version table. Comprehensive information on in-progress and built wind turbine locations originated from the Federal Aviation Administration Obstruction Evaluation/Airport Airspace Analysis was provided to NSSL by the Radar Operations Center. Additional information was gathered from the American Wind Energy Association, Alternative Energy Institute, Kansas Energy Information Network, Great Plains Energy Corridor, Massachusetts Government, U.S. Department of Energy New England Wind Forum, and Iowa State University/Iowa Energy Center. Existing wind turbine locations were also identified or verified using the imagery in online map servers such as Google Maps and Environmental Systems Research Institute's ArcGIS Online.

After wind turbine locations were identified, the clutter contamination region is determined using 12-month accumulated precipitations estimated by MRMS (Zhang et al. 2016). In the current work, the mean (μ_{rain}) of QPE accumulation was calculated in an area around each

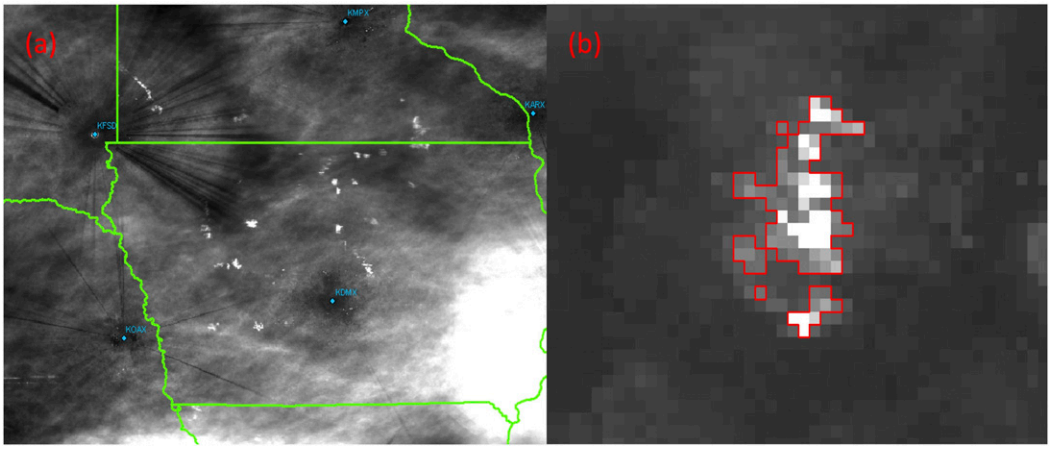

FIG. 3. (a) The region of possible wind turbine clutter identified from exceptionally high values in a 12-month MRMS precipitation estimate accumulation. (b) Polygons delineating an area of wind turbine clutter.

wind farm. Any radar gate associated with an anomalously high accumulation ($>2\mu_{rain}$) is determined as the possible wind turbine clutter region (Fig. 3a). The possible clutter area was delineated with a polygon (Fig. 3b) that was then included in a wind turbine clutter shapefile for the CONUS.

The negative impact of wind farms on weather radars decreases exponentially as a function of the distance to the radar. The impact distance is highly dependent on local terrain and radar propagation (Vogt et al. 2011). Given windmills' heights and possible AP of radar beams, a list of windmills within an 80-km range is created for each radar. The simple-format tables include the identity number (ID) and location information of each WF center regarding azimuth angle (°) and range (km). The power returns are identified as possibly contaminated at these designated locations.

2) CORRECTION ON THE WIND FARM VOIDS

The contaminated radar returns from the wind turbine regions have different severity levels depending on the environmental conditions and radar beam propagation. The downward AP radar beam would worsen the clutter contamination. In another scenario, the echoes from the wind turbines do not appear distinguished from the neighboring echoes of heavy convective storms. For example, Fig. 4 demonstrates an event of WF clutter embedded inside the precipitation echoes observed by radar KVNX on 7 June 2014. The WF contamination appears severe at 0623 UTC shown in Figs. 4b and 4d, while the visual impact in Z is minor in the scans at 0712 UTC (Figs. 4e,f). The white ellipses mark the locations identified in the WF table. The six plots are from two scans: 1) at 0623 UTC, raw Z with marked WF locations (Fig. 4a), raw Z before WF correction (Fig. 4b), the associated ρ_{HV} (Fig. 4c), the Z field after the QC process (Fig. 4d); 2) at 0712 UTC, the raw Z where no WF correction is needed (Fig. 4e), and the associated ρ_{HV} (Fig. 4f). In this work, the pixels from the WF area are classified into different groups and processed separately.

Centered at each of the WF locations, the WF neighboring regions are defined as near neighbor (8 km × 10°) (purple areas inside the white ellipse in Fig. 4a) and far neighbor (12 km × 12°) (outer layers around the purple regions in Fig. 4a). The near-neighboring area is vulnerable to the WF contamination under AP propagation, while the far-neighboring area does not contain WF clutter. Generally, the WF clutter is associated with large spatial variability (SPIN) of the reflectivity field (Steiner and Smith 2002), enhanced Z (Fig. 4b), and decreased ρ_{HV} (Fig. 4c) within the near-neighboring region. Isolated clutter also shows a lack of reflectivity continuity in the vertical direction. In situation 1, the nonmissing echoes, associated with lower ρ_{HV} than light rain, are observed inside the near-neighbor area while with a clean far-neighbor region. These isolated echoes are possible residual WF clutter or mixed with small-size convective cells. For a radar echo that is associated with lower ρ_{HV} (<0.98) in the near-neighboring region, the corresponding echo top of 18 dBZ is checked by going through higher tilts (Tang et al. 2016). Potential storm cells of a mixture of hail/rain are associated with a high echo top (>6 km) and will be retained; otherwise WF clutter will be removed entirely. In situation 2, the WF contamination is embedded in the precipitation returns when the near-neighboring and far-neighboring regions are filled with returns from precipitation targets, turbine blades, or the mixture (Fig. 4). Under this situation, the local texture of the Z and ρ_{HV} values show visible contamination in

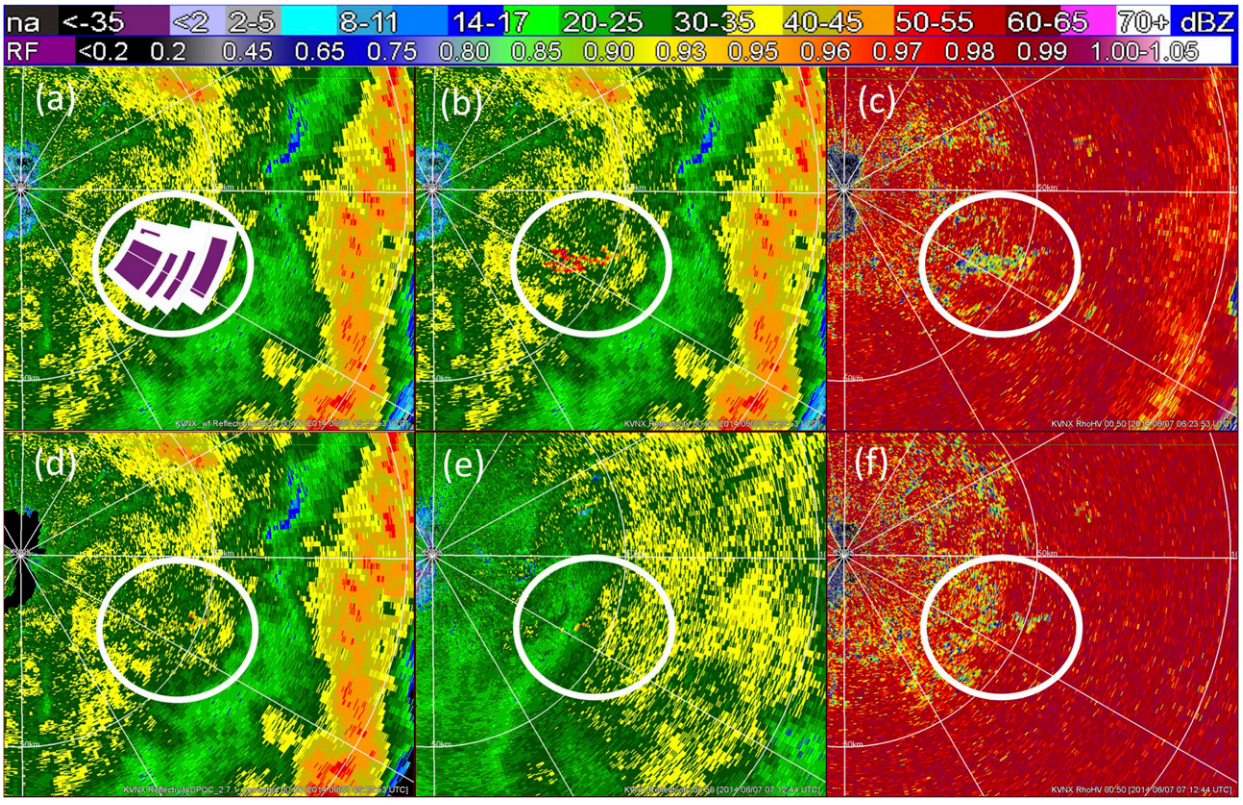

FIG. 4. A precipitation event observed by the radar at Vance Air Force Base (KVNX) at 0.5° elevation angle on 7 Jun 2014, where the white ellipses mark the locations identified in the WF table. (a)–(d) Observations at 0623 UTC: (a) raw Z with marked WF locations, (b) raw Z before WF correction, (c) the associated ρ_{HV}, and (d) the Z field after the *dpQC2* process. Inside the white ellipse in (a), the purple areas are the nearest-neighbor region, and the whited-out layers are the far-neighbor regions centered at the WF locations. (e)–(f) Observations at 0712 UTC: (e) the raw Z where no WF correction is needed, and (f) the associated ρ_{HV}. The color scales of Z and ρ_{HV} fields are shown at the top of the figure.

each WF location near-neighbor region. If the low ρ_{HV} ($<$0.98) bins number is equal or larger amount than the high ρ_{HV} ($\geq$0.98) bins inside the near neighbor (purple rectangles in Fig. 4a), it is an indication of a possible mixture of the returns from meteorological targets and WF clutter. The average Z value within the near neighbor is compared with the measurement from the far-neighboring echoes (white layers in Fig. 4a). In the radar scan at 0712 UTC (Figs. 4e,f), the difference of the average Z values are small ($<$10 dBZ) between the near-neighbor and far-neighbor regions, and the bias is considered minor; therefore, no correction was made. Otherwise, the pixels associated with decreased ρ_{HV} and large SPIN are flagged as WF contamination. Complete removal of the biased echoes leaves voids in the reflectivity maps; therefore, the contaminated echo is replaced using the mean value of the far neighbors. A correction is applied when the mean value from the near neighbors is much higher than the far neighbors ($\geq$10 dBZ). In Fig. 4d, the pixels with highly biased reflectivity are corrected.

The dpQC removes the majority of nonprecipitation echoes from WF areas, and the dpQC2 updates apply WF tables further clear the occasional residual clutter. When the clutter echoes are embedded in storms, the dpQC2 corrects the biased echoes using the mean nearby measurement if severe WF contamination is observed. It leaves the echoes retained if there are no evident changes in the intensity of texture at the WF locations. The QC refinement benefits the accumulated QPE products in the MRMS system.

c. *Quality control with the degraded noise level*

1) IMPACT AND IDENTIFICATION OF THE BIASED HORIZONTAL/VERTICAL NOISE LEVEL

Generally, noise levels in horizontal (H) and vertical (V) channels are stable, and their variations show consistency. Degraded noise information in any channel cause biases in radar data, and such phenomena have been observed in WSR-88Ds during real-time operations. The degraded noise in the H channel impacts

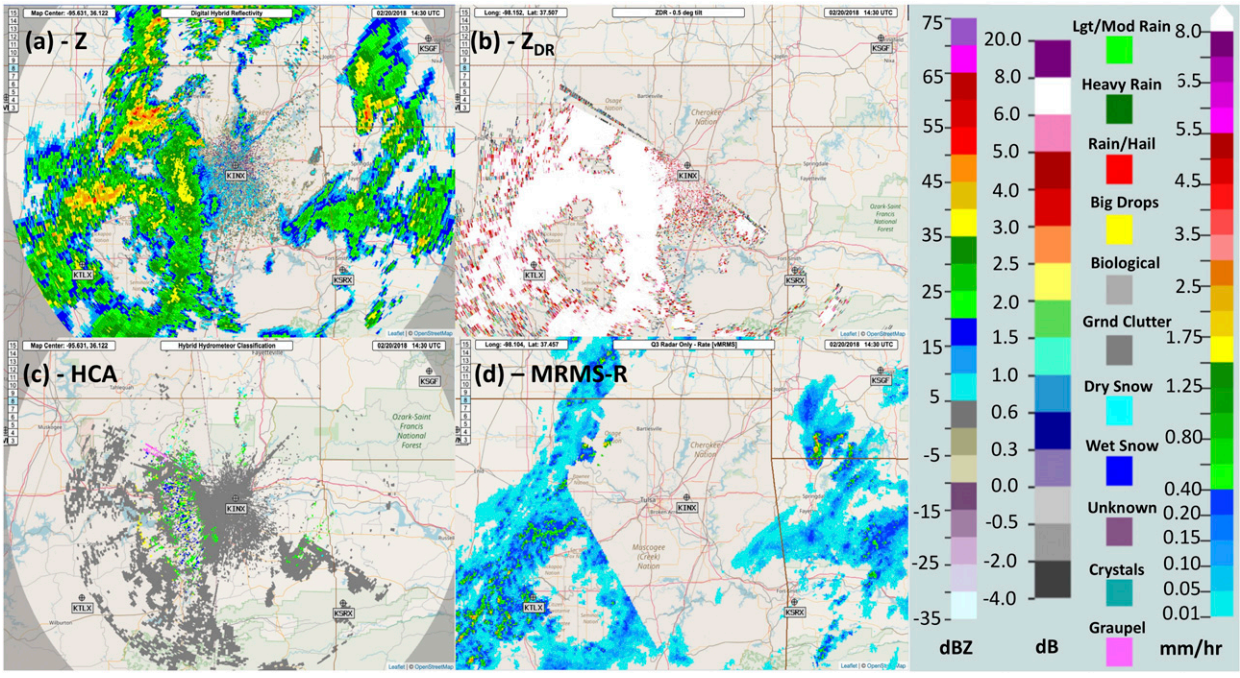

FIG. 5. The observations when the noise data were degraded. (a)–(c) Single radar measurements and derivations from Tulsa (KINX) at 1430 UTC 20 Feb 2018: (a) Z, (b) Z_{DR}, and (c) the derived hydrometeor classification (HCA). (d) The MRMS mosaicked field of rain rate (MRMS-R). The color scales of the products in (a)–(d) are listed from left to right, respectively, beside the four panels. In these panels, the Z field in (a) shows reasonable values, but Z_{DR} in (b) is contaminated. The degradation of the input data leads to the HCA in (c) of a false classification in the precipitation categories and the MRMS-R in (d) of biased estimation.

the estimated Z field, while the degradation of the V channel noise impacts the differential reflectivity (Z_{DR}) and ρ_{HV} (M. Simpson et al. 2019, unpublished manuscript). Consequently, it biases modules and products, including radar QC processes, hydrometeor classification, QPE, and flash flood warnings. Figure 5 shows examples of polarimetric variables, hydrometeor classification results, and rain rate estimations, respectively. The radar data are observed at Tulsa, Oklahoma (KINX), at 1430 UTC 20 February 2018. Although Z fields (Fig. 5a) are in the reasonable range, the Z_{DR} (Fig. 5b) values reach, 6 dB for most of the regions, much higher than normal values for typical hydrometeors. Because of the biased measurement in the polarimetric variables, the operational product of hydrometeor classification derived by the National Weather Service (Fig. 5c) did not correctly classify the precipitation categories. It also affected the MRMS precipitation products, i.e., the mosaicked field of rain rate, shown in Fig. 5d. The MRMS rain rate grids are derived using the mosaicked reflectivity field generated from individual radars (Zhang et al. 2016). The biased dual-polarization variables caused false alarms in the QC process on KINX. The falsely removed radar data in the mosaicked field negatively impacted on the MRMS QPE products. A special QC process is applied to avoid the adverse effects of these abnormal channel noises on downstream products.

Simpson et al. (2019) developed a novel approach to diagnose real-time instances of degraded H and/or V channel noise. Based on the azimuthal H and V noise values, the azimuth is flagged as degraded if the H or V noise for a given azimuth on a given tilt exceeds 1.5 ± mean H noise or 1.5 ± mean V noise. The mean H/V noise is the mean value of the H/V noise within a given full volume scan. The bad radials are flagged in real-time and provide a reference input to the QC process. Figure 6 shows the example outputs of the noise monitor in the MRMS system.

2) SINGLE-POLARIZATION QC FOR V NOISE CONTAMINATION

The degraded V channel noise impacts the dual-polarimetric values such as Z_{DR} and ρ_{HV} but does not have significant impacts on the horizontal data such as Z, V_r, and σ_v. Figure 7 shows examples of radar variables collected by the radar at Chicago, Illinois (KLOT), at 1356 UTC 5 April 2018. The fields of Z, ρ_{HV}, Z_{DR}, V_r, and σ_v are shown in Figs. 7a–e, respectively. When the V channel noise is degraded, the biased polarimetric fields of ρ_{HV} and Z_{DR} (Figs. 7b,c) lead to a failure of the dpQC algorithm. On the other hand, the fields

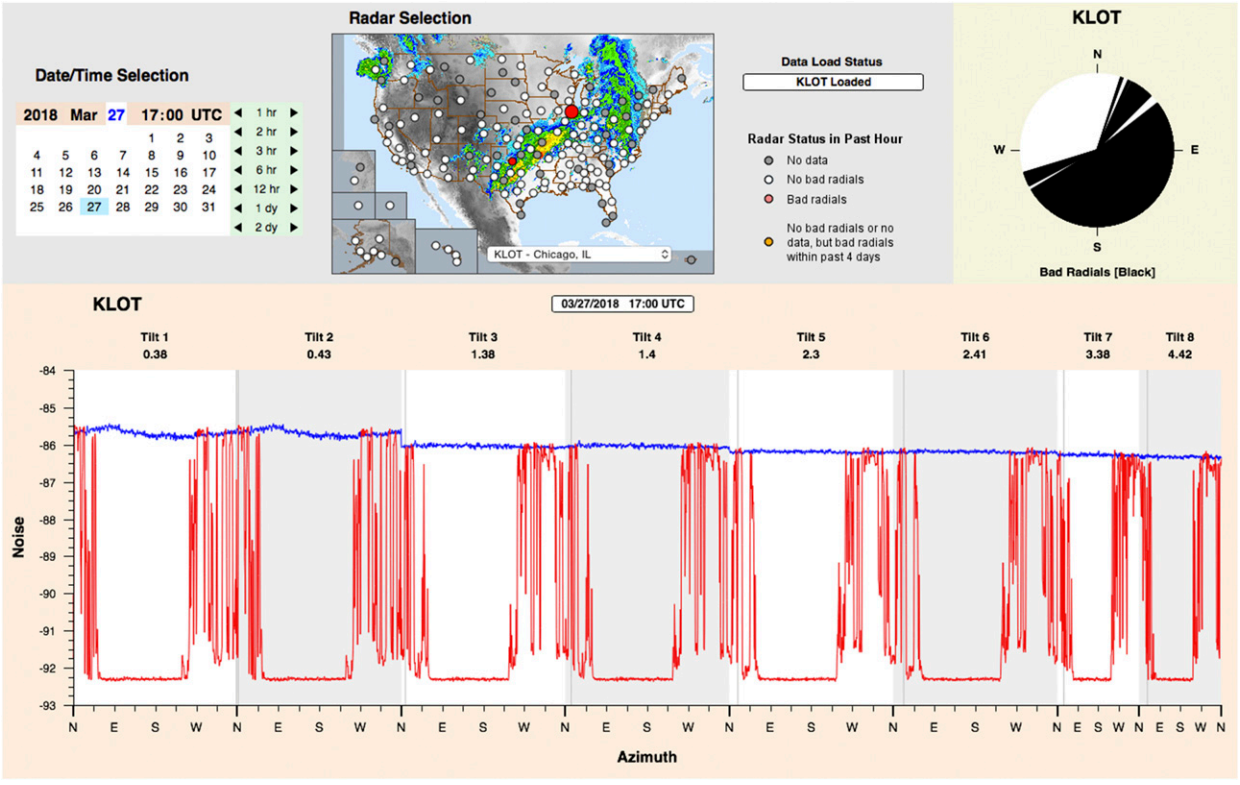

FIG. 6. Real-time monitoring system of the biased noise level. (top left) Selecting the radar and time, (top right) using Chicago (KLOT) as an example, (bottom) the noise levels at each tilt are shown. The blue and red lines are the horizontal and vertical noise (dBm), respectively. The x axis is the radial direction on each tilt. In the degradation directions (the most east and south regions), the asymptotic bottoming-out of the horizontal and vertical channels can be observed. The impacted radials are identified with the black color shown in the top-right image.

estimated from the H channel show reasonable values in this case (Figs. 7a,d,e).

To identify nonprecipitation echoes from precipitation radar echoes when the V noise degradation is detected, a Bayesian quality control (bqc) method was developed in the current work. Comparing to other clutter identification algorithms in single-polarization radars (i.e., Bachmann and Tracy 2009; Lakshmanan et al. 2012; Steiner and Smith 2002), the proposed approach has a simple framework and less computational cost, therefore, could be an optimal candidate of the supplements of the dpQC.

The bqc takes Z, V_r, and σ_v as inputs and classifies the radar echoes into either precipitation or nonprecipitation. It applies the idea of the naïve Bayes theorem (Walpole et al. 2016), while instead of the real probability, it scores the classes using Eq. (4):

$$P(c|x) = P(x_1|c)P(x_2|c)P(x_3|c), \tag{4}$$

where x_1, x_2, and x_3 are the predictors (Z, V_r, and σ_v), and c is the class (c_1: precipitation; c_2: nonprecipitation). In Eq. (4), $P(c|x)$ is the posterior score of the class. For the given c (class), $P(x|c)$ is the conditional score applying a function of half-Gaussian half constant. Equation (5) shows $P(Z|c_1)$ as an example:

$$P(Z|c_1) = \begin{cases} \dfrac{1}{\sqrt{2\pi\sigma^2}} \exp\left[\dfrac{-(x-\mu)^2}{2\sigma^2}\right] & x \le \mu \\ \dfrac{1}{\sqrt{2\pi\sigma^2}} & x > \mu \end{cases}, \tag{5}$$

where μ and σ are the mean and standard deviation estimated from the precipitation returns in the training data. Oppositely, the conditional score of $P(Z|c_2)$ uses the half-Gaussian function in the higher value end and the constant at the lower value end. The similar functions are also applied to predictors V_r and σ_v. Since the instances of noise degradation occasionally occur (Simpson et al. 2019), the parameters of likelihood are trained and updated using the uncontaminated data from the previous scan with no degradation in the dual-polarization variables when the dpQC performs a full function in identifying the

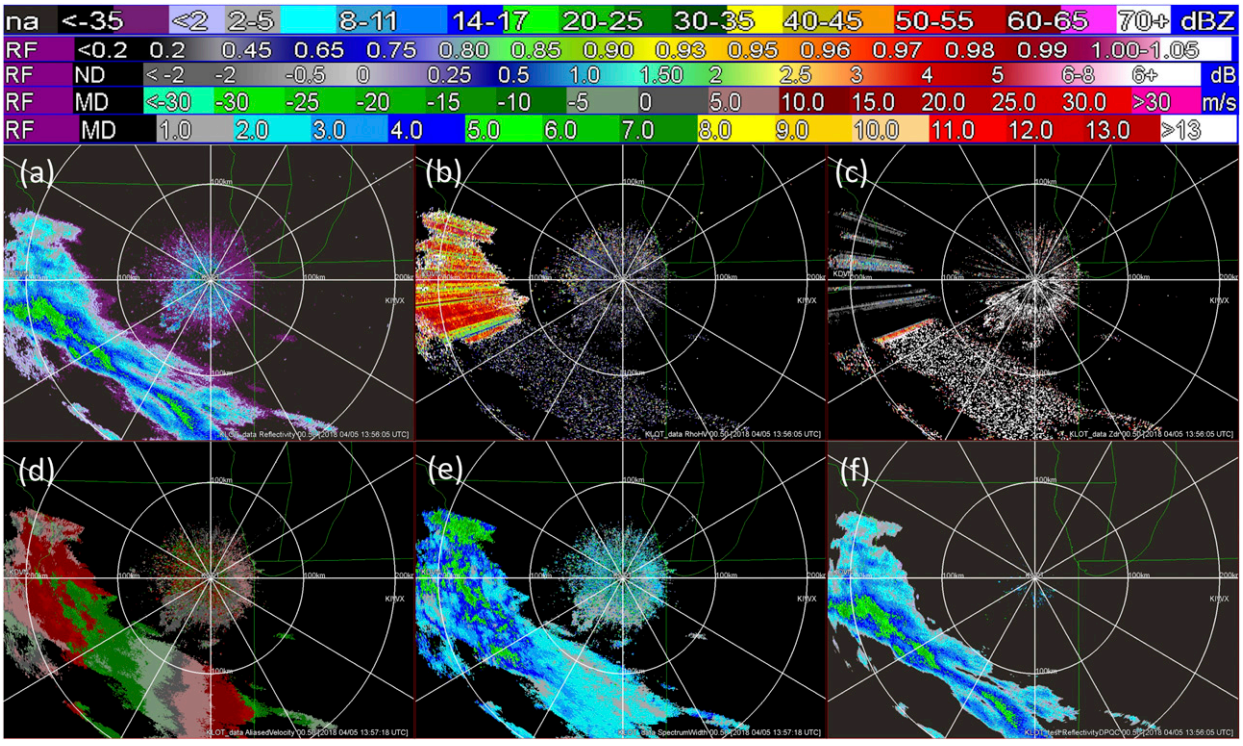

FIG. 7. Contaminations in dual-polarization variables are observed in the radar at Chicago (KLOT) at 1356 UTC 5 Apr 2018. (a)–(e) The level-II data of Z, ρ_{HV}, Z_{DR}, V_r, and σ_v, respectively. Biased measurement is observed in the polarimetric fields of (b) ρ_{HV} and (c) Z_{DR} but not in the Doppler variables (a) Z, (d) V_r, and (e) σ_v. (f) When the polarimetric variables are contaminated, the bqc applies the Doppler variables to deliver the quality-controlled Z maintaining the precipitation information clear of clutter. The color maps of Z, ρ_{HV}, Z_{DR}, V_r, and σ_v are listed from top to bottom, respectively, above the panels.

nonprecipitation clutter. The statistical μ and σ of the precipitation and clutter classes are recorded, and they are applied when the polarimetric variables are degraded, i.e., the statistics derived from the earlier scan is used to identify the clutter at the current scans if the contamination is identified. The bqc takes advantage of the weather consistency to classify the precipitation and nonprecipitation echoes. Therefore, it is limited in removing the instantaneous clutter or the applications over a long gap in time. The bqc is able to identify the majority of nonprecipitation clutter and the remained clutter removed through checking the reflectivity texture. In regions close to the radar, a vertical gradient test is employed to check the vertical continuity of echoes at the lowest tilts. The echoes are identified as clutter if their intensities dramatically decrease in height (i.e., $>50\,\mathrm{dBZ\,km^{-1}}$). The checking window is a box of 1.25 km $\times$ 1.5 azimuth degrees centered at every nonmissing reflectivity bin. If more than one-half bins have missing values or the averaged reflectivity of the adjacent nonmissing bins is less than 25% of the center bin's reflectivity, this center pixel is considered as noise or AP and removed.

The performance of the proposed complementary QC was demonstrated in Fig. 7. In this case, the polarimetric variables ρ_{HV} and Z_{DR} show significant biases because of the degraded noise level in the V channel (Figs. 7b,c). The biased measurements will cause failures in polarimetric quality control approaches (such as dpQC). The proposed bqc, on the other hand, provides reasonable quality control results, as shown in Fig. 7f. It can identify and remove the majority of the biological clutter near the radar site using the Doppler variables (Figs. 7a,d,e).

3) DISABLE THE RADAR DATA APPLICATION FOR H NOISE CONTAMINATION

Although observed rarely, the degraded H noise is also found in the operational system (Simpson et al. 2019). Under this situation, not only the dual-polarization variables are contaminated but also the Doppler measurements in the horizontal direction, including Z. Because all inputs are problematic, the corrupted radar data are removed from the radar network to avoid contamination in the downstream processing. In the mosaicked QPE field, the void area from removing the

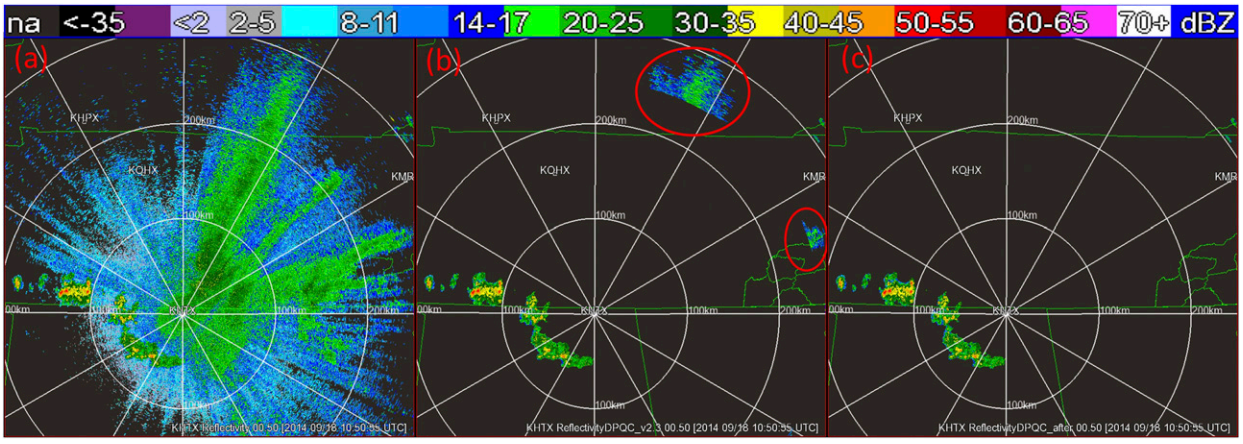

FIG. 8. (a) The raw base reflectivity field from Huntsville, Alabama (KHTX), at 0.5° elevation angle, (b) the reflectivity field after the dpQC process, and (c) the field processed by dpQC2. The red ellipses highlight the residual clutter at far ranges that were completely removed. The fields are observed at 1050 UTC 18 Sep 2014.

corrupted data is filled with the estimations from adjacent radars.

d. Other improvements in WSR-88Ds

When ground clutter and biological returns combine with AP, these nonprecipitation echoes could appear at farther ranges and higher tilts than their actual locations (Fig. 8a). It has been challenging to identify such nonprecipitation echoes when they are embedded in precipitation echoes near the ML. An integrity check near the ML bottom is added to avoid the artificial edges caused by partial removal of the clutter (Fig. 8b). Based on the characteristics of Z and ρ_{HV} fields, the echoes are segmented into groups along with radial directions. If ground/biological clutter is identified below the ML, the echoes from the same section are also cleared, even they extend beyond the ML height (Fig. 8c). The dpQC2 algorithm can further remove the residual clutter when they appear at a high altitude/far range.

The sun spike is associated with low ρ_{HV}. When the sun spike is embedded among precipitation echoes (Fig. 9a), the sun spike removal would leave a spike gap (Fig. 9b). In the QC refinement, the gap pixels are recovered with the original value when the sun spike is surrounded by the weather information (Fig. 9c).

e. Canadian radar QC update

1) COMBINATION OF DOPVOL AND CONVOL DATA

Different from typical volume coverage patterns (VCP) operated in the United States, Canadian radars complete

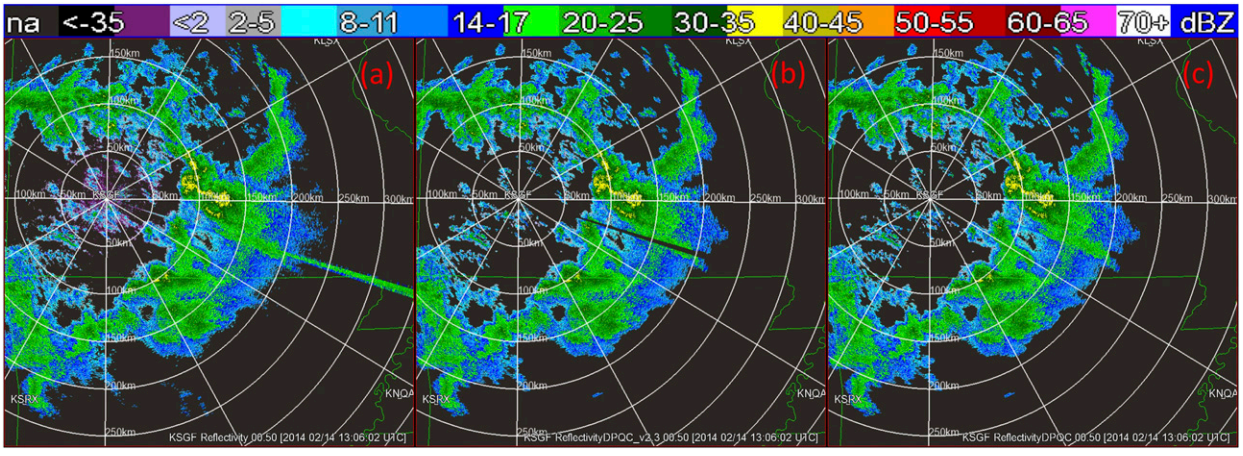

FIG. 9. (a) The raw Z field observed by the radar at Springfield (KSGF) at 1306 UTC 14 Feb 2014, (b) the Z field processed by dpQC, and (c) the Z field processed by dpQC2. In this case, the update recovers the precipitation echoes that mixed with sun spike clutter.

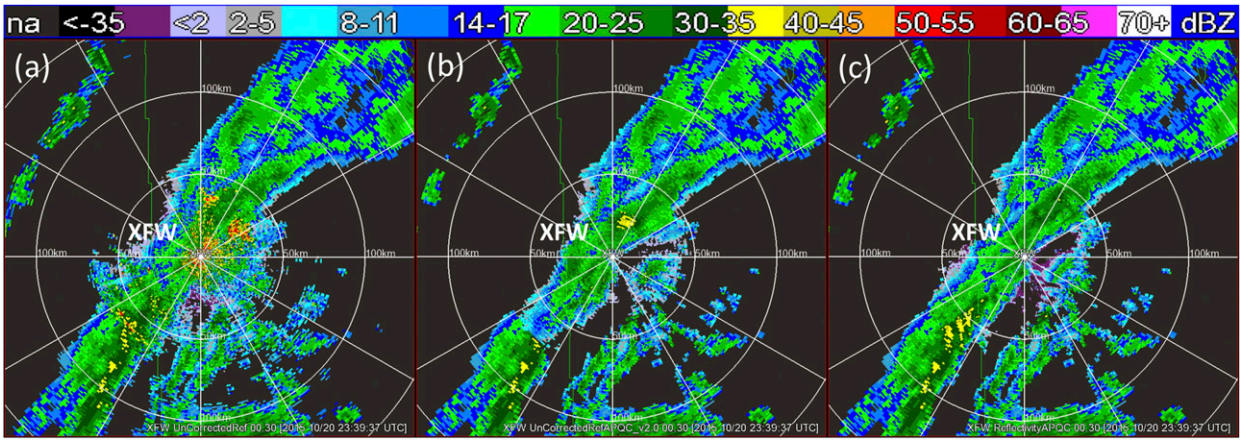

FIG. 10. A case when AP and regular ground clutter mixed with precipitation echoes observed by Brandon (XFW) at 2339 UTC 20 Oct 2015. (a) The raw Z field at 0.5° elevation angle, (b) the result corrected with the CONVOL data from a higher tilt, and (c) the result corrected with the data from the Doppler scans.

one-volume scan in 10 min. Each volume consists of 24 tilts, and only 3 of them associated with Doppler measurements. The full three-dimensional volume scan (CONVOL) base-level data are used in creating the three-dimensional reflectivity grid and QPE (Tang et al. 2016) in the MRMS system. Due to negative-elevation-angle-scans and limited quality control of level-I signal processing in Canadian radars, the ground clutter has significant impacts on CONVOL data. Although the clutter mitigation scheme can identify and remove the ground clutter, it will leave voids in the rain rate field when the clutter is embedded in precipitation echoes.

In the early version Canadian radar QC, the voids were corrected using the reflectivity values at higher tilts from the CONVOL data. Figure 10b shows an example scan observed by the radar at Brandon, Manitoba (XFW), at 2339 UTC 20 October 2015. However, the adoption of reflectivity data using higher tilts potentially leads to inaccurate rainfall rate estimation inside the void regions. For example, the reflectivity field after the quality control in Fig. 10b mitigates the ground clutter observed in Fig. 10a, where the higher tilts field was applied in the void region. The corrected field (Fig. 10b) shows dampened intensity at the range of 50 km southwest to the radar site, which would directly lead to rainfall rate underestimation in shallow precipitation. On the other hand, the Doppler volume scans (DOPVOL) contain the moments of velocity and spectrum width. By analyzing spectral domain with filter functions, the processed reflectivity data in DOPVOL mitigate the clutter's adverse effect with the less degrading quality of meteorological data. However, the DOPVOL data are available only at the lowest three elevation scans with different resolutions and ranges from the CONVOL data. In the update of Canadian QC, the reflectivity field from CONVOL volume is combined with Doppler variables considering the time shifts between their scans, the difference of their scanning elevation, as well as the field resolution and range. Figure 10c shows the combination of the CONVOL and DOPVOL data contains ample volume coverage and reasonable clutter identification and correction near the radar site.

2) LAKE/SEA CLUTTER MITIGATION

The radars at Montreal River (WGJ) and Val d'lrene (XAM) suffer lake/sea clutter, especially when radar beams anomaly propagate. Figure 11b demonstrates an example of the reflectivity field contaminated with severe clutter from the Lake Superior, observed by WGJ at 2019 UTC 9 February 2017. It is challenging to remove the clutter completely, especially under the winter VCP where the scanning tilt could be as low as 0.2° for WGJ and −0.5° for XAM. The contamination is observed in both CONVOL and DOPVOL data. In the update of Canadian QC, the reflectivity from the lowest four tilts were collected at the lake regions. The potential clutter contamination is identified when the reflectivity intensity has a fast deduction along with the vertical height. The echoes from higher tilts were applied in the correction to mitigate the overestimation of the rainfall rate due to the mixture of precipitation echoes and lake clutter (Fig. 11c).

3. Real-time performance

The performance of the updated dpQC2 was validated in real-time on the MRMS system. A 4-yr evaluation (from 2015 to 2019) found the updated dpQC2 shows enhanced performance in robustness and accuracy compared to the dpQC. Figure 12 shows an example of the

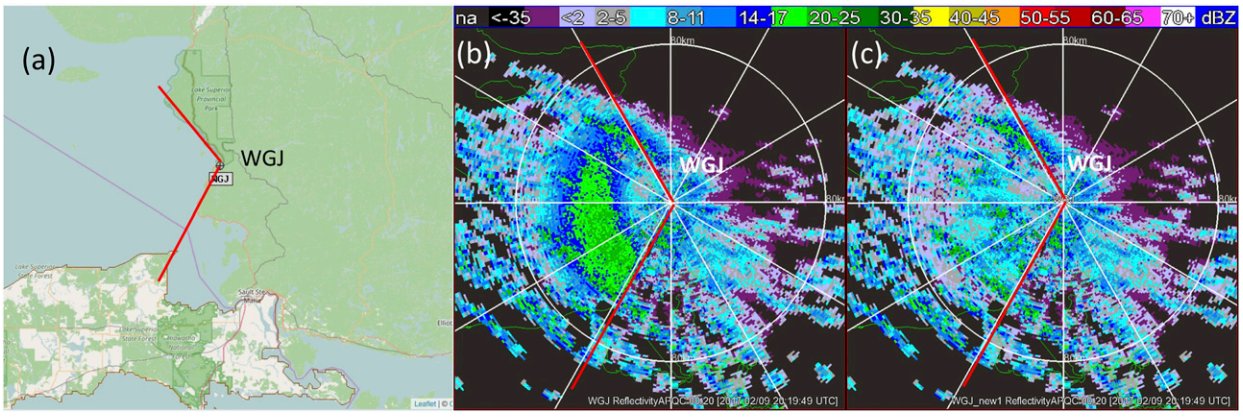

FIG. 11. (a) The location of radar WGJ at Montreal River and the surrounding environment; (b) the reflectivity field at 0.2° elevation after the process of dpQC at 2019 UTC 9 Feb 2017, where sea clutter still can be observed; and (c) the sea clutter is mitigated using the dpQC2.

performance at 0500 UTC 30 May 2015. Figure 12a is the mosaicked composite reflectivity (CREF) field across CONUS before the QC process; Fig. 12b is the CREF field processed by dpQC; and Fig. 12c is the CREF field processed using the updated dpQC2. Observing Figs. 12b and 12c, the red and white ovals point out some of the differences in the regions of radars at Rapid City, South Dakota (KUDX), Brownsville, Texas (KBRO), El Paso, Texas (KEPZ), and Laughlin AFB, Texas (KDFX). The echoes around KUDX and KBRO (red ovals) are removed by dpQC2 (Fig. 12c), while the echoes close to KEPZ and KDFX (white ovals) are retained compared to Fig. 12b. The quality-controlled results are further validated with ground gauge measurements, and no precipitation is observed around KUDX and KBRO within the time frame. It shows that the refined algorithm shows enhanced quality control in removing biological clutter close to the radar site and better retaining the precipitation echoes.

To quantitatively measure the influence of the updated QC algorithm on the QPE products, a comparison between radar QPE and gauge measurement over a 5-day (20–24 February 2018) time window is presented in the current work. During this period, the hardware

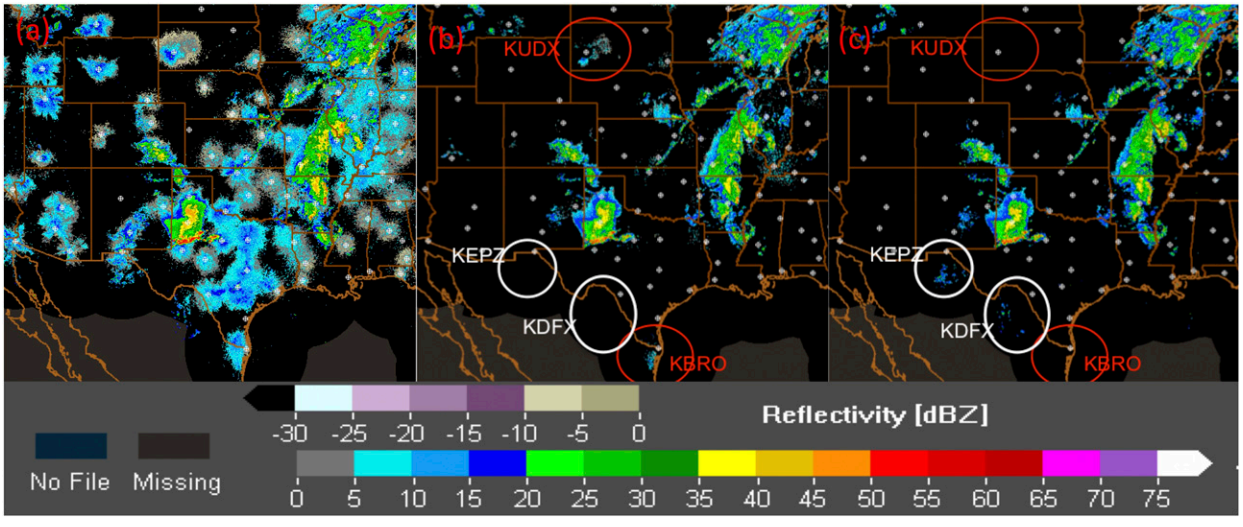

FIG. 12. (a) The mosaicked composite reflectivity (CREF) field across CONUS before any QC process, (b) the CREF field processed by dpQC, and (c) the CREF field processed using dpQC2. The fields are observed at 0500 UTC 30 May 2015. The red ovals highlighting the residual echoes around KUDX and KBRO are removed in (c). The the white ovals show the echoes close to KEPZ and KDFX are retained in (c).

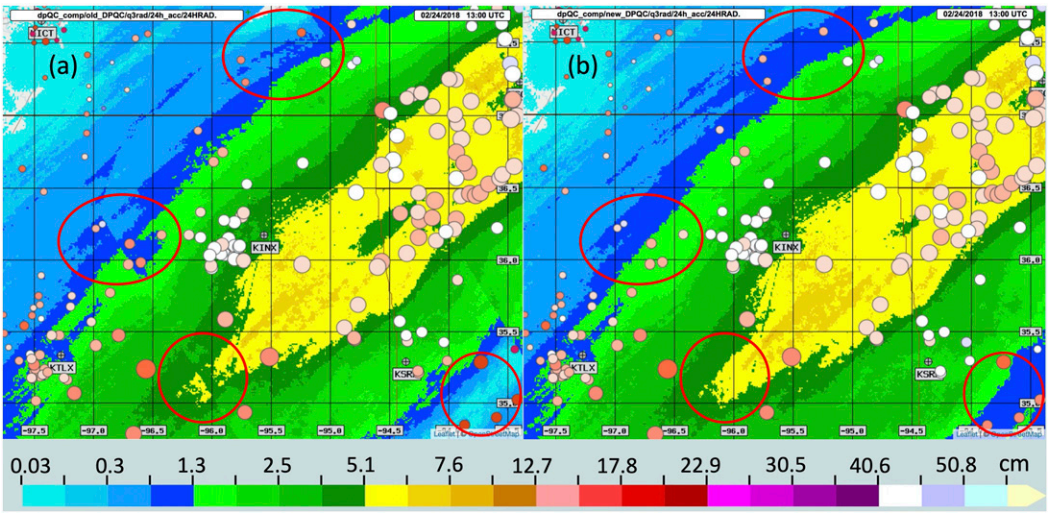

FIG. 13. The gauge measurements on top of the 24-h accumulated QPE field derived from the radar Z field processed by (a) dpQC and (b) dpQC2 at 1300 UTC 24 Feb 2018. The bubble size is proportional to the gauge measurement, and the bubble color indicates the bias of QPE. The warm color (red) represents an underestimation, cool color (blue) shows an overestimation, and the neutral color (white) implies the perfect match. The validation data are collected from six radars at Wichita (KICT), Vance Air Force Base (KVNX), Oklahoma City (KTLX), Tulsa (KINX), Fort Smith (KSRX), and Springfield (KSGF). The ground observation is from daily Community Collaborative Rain, Hail and Snow Network (CoCoRaHS) gauges.

issues were observed from the radar at Tulsa, which leads to the enhanced bias in rain rate estimation. Figure 13 shows the selected domain at the central United States covering +34.75° to +37.75° latitude and −93.40° to −97.75° longitude. The validation data are collected from six radars at Wichita, Kansas (KICT), Vance Air Force Base, Oklahoma (KVNX), Oklahoma City, Oklahoma (KTLX), Tulsa (KINX), Fort Smith, Arkansas (KSRX), and Springfield, Missouri (KSGF), respectively. The ground observation is from daily Community Collaborative Rain, Hail and Snow Network (CoCoRaHS) gauges. In the evaluation, the individual radar data were first processed with the original dpQC (Tang et al. 2014) and the proposed dpQC2. The quality-controlled radar fields from individual radars were then mosaicked, and the radar QPE was calculated using the approach proposed by Zhang et al. (2016). The multiple R–Z relationships [Eqs. (1)–(6) in Zhang et al. 2016] were used to compute the surface precipitation rate for different precipitation types (Fig. 10 in Zhang et al. 2016). The 24-h accumulated radar rain rate or snow water equivalent was compared with the gauge network observations.

Figure 13 presents a pair of example fields at UTC 1300 24 February 2018, where the gauge measurements are shown as colored bubbles on the top of the 24-h accumulated QPE field derived from the radar Z field processed by dpQC (Fig. 13a) and dpQC2 (Fig. 13b). The bubble size indicates the measurement value. The bubble color indicates the QPE bias: the warm color (red) is underestimation, cool color (blue) shows overestimation, and the neutral color (white) implies the match. Within the 5-day testing time window, a total of 1013 pairs of QPE and gauge measurement are used in the statistics. Statistical measurements score the validation of the radar rainfall estimation: the average bias, the mean absolute error (MAE), and the correlation coefficient (CC) (Ryzhkov and Zrnić 2019). During the study period, the noise degradation of the vertical channel noise is identified from radar KINX. The contamination in the polarimetric measurements negatively impacted the dpQC performance. Some precipitation returns are falsely removed due to the degraded ρ_{HV} and other polarimetric variables. Although the multiple radar mosaicking scheme took advantage of the observation from neighboring radars to mitigate the underestimation, the mean bias of the QPE estimation over gauge measurement is 0.883. The updated dpQC2 involves a supplementary single-polarization QC and improves the robustness in real-time performance. As highlighted with the red ovals, the dpQC2 reduced the discontinuities in the QPE field and mitigated the underestimation (Fig. 13b). As a result, the product derived from the dpQC2 has an enhanced mean bias of 0.900; the MAE decreased from 0.428 to 0.412 cm. The CC improvement is slight from 0.859 to 0.860. The updates are able to ensure a consistent QC performance during the incidental data corruption. The updates not only improve

the radar-based QPE but also benefit the downstream applications in hydrological modeling.

4. Summary and discussion

The radar data QC algorithm directly impacts the quality of the MRMS three-dimensional radar mosaic and the severe weather and precipitation product suites. The three-dimensional mosaic product is used in the operational HRRR model; therefore, its quality can impact the data assimilation and accuracy of the quantitative precipitation forecasts. The MRMS severe weather products are used by the NWS weather forecast offices (WFOs) for real-time situational awareness, and the precipitation products are used for flash flood warnings at the WFOs and as forcing to the operational hydrological models at the River Forecast Centers and National Water Center. Misdetection of the ground clutter in the dual-polarization QC could result in false precipitation forecasts and overestimation bias in streamflow predictions. Erroneous removal of weather echoes could potentially result in missed detection of severe weather and underestimation in streamflow predictions.

Several major updates to the radar QC are implemented in the MRMS system, and their impacts are presented in this paper. The updated dpQC2 algorithm provided the following improvements: 1) better-preserving precipitation echoes by more accurately locating the melting layer associated with the decreased correlation coefficients, 2) identifying wind farm clutter and correcting the biased reflectivity associated with WFs embedded in precipitation, 3) minimizing impact of the corrupt data related with radar hardware issues, 4) further reducing the residual clutter from biological migration and/or due to anomalous propagation of the radar beams, and 5) further reducing lake/river clutter from specific Canadian radars.

Compared to existing approaches, the proposed updates highlight the novelty in three aspects. First, the two-dimensional freezing-level field, derived from a combination of the HRRR and the RAP model analyses, combined with radar observations, is applied in the melting-layer detection for the first time. Second, the radar hardware issue of noise level degradation was addressed using an approach based on the Bayes theory. The proposed bqc is straightforward and able to provide a consistent quality control result when the dual-polarization variables are biased. Third, different from the methods of signal processing schemes, the proposed update mitigates the WF contamination in level-II radar data. It not only identifies the contamination region through a lookup table and radar data but also provides a set of correction schemes depending on the contamination severity. The QC updates showed statistical improvements in reducing nonprecipitation clutter and better retaining the weather information. The real-time process accommodates the costs and benefits of the computational resource since it is running upon over 140 radars in the CONUS. They are designed to improve the QC robustness in different issues for individual radars with an economic computational cost. For example, by applying the referential location tables, the mitigation of the WF contamination can handle individual radars efficiently with minimum impact of the QC process in other radars. The bqc scheme works as a quick substitute to avoid false alarms due to biased radar measurements. The proposed refinements are able to extendedly improve the quality control of the radar data in the MRMS system.

Due to the range difference between the polarimetric variables, such as ρ_{HV} (300 km) and reflectivity field (460 km) of the WSR-88Ds, it is still challenging for the clutter at a range further than 300 km away from the radars due to anomalous propagation. Some residual clutter, while infrequent, may still be seen far offshore, and additional data sources (e.g., satellite) may be needed to reduce these nonprecipitation echoes further.

Acknowledgments. The authors thank three anonymous reviewers for their thoughtful reviews and comments on this manuscript.

REFERENCES

Andrić, J., M. R. Kumjian, D. S. Zrnić, J. M. Straka, and V. M. Melnikov, 2013: Polarimetric signatures above the melting layer in winter storms: An observational and modeling study. *J. Appl. Meteor. Climatol.*, **52**, 682–700, https://doi.org/10.1175/JAMC-D-12-028.1.

Bachmann, S. M., and M. Tracy, 2009: Data driven adaptive identification and suppression of ground clutter for weather radar. *25th Conf. on Int. Interactive Information and Processing Systems for Meteorology, Oceanography, and Hydrology*, Phoenix, AZ, Amer. Meteor. Soc., 11B.3, https://ams.confex.com/ams/89annual/techprogram/paper_146356.htm.

——, Y. Al-Rashid, P. Bronecke, R. Palmer, and B. Isom, 2010: Suppression of the wind farm contribution from the atmospheric radar returns. *26th Conf. on Interactive Information and Processing Systems for Meteorology, Oceanography, and Hydrology*, Atlanta, GA, Amer. Meteor. Soc., 392, https://ams.confex.com/ams/90annual/techprogram/paper_159956.htm.

Balakrishnan, N., and D. S. Zrnić, 1990: Use of polarization to characterize precipitation and discriminate large hail. *J. Atmos. Sci.*, **47**, 1525–1540, https://doi.org/10.1175/1520-0469(1990)047<1525:UOPTCP>2.0.CO;2.

Benjamin, S. G., S. Weygandt, T. G. Smirnova, M. Hu, S. E. Peckham, J. M. Brown, K. Brundage, and G. S. Manikin, 2009: Assimilation of radar reflectivity data using a diabatic digital filter: Applications to the Rapid Update Cycle and Rapid

Refresh and initialization of High Resolution Rapid Refresh forecasts with RUC/RR grids. *13th Conf. on Integrated Observing and Assimilation Systems for Atmosphere, Oceans, and Land Surface*, Phoenix, AZ, Amer. Meteor. Soc., 7B.3, https://ams.confex.com/ams/pdfpapers/150469.pdf.

——, ——, C. Alexander, J. M. Brown, T. G. Smirnova, P. Hofmann, E. James, and G. Dimego, 2011: NOAA's hourly-updated 3km HRRR and RUC/Rapid Refresh—Recent (2010) and upcoming changes toward improving weather guidance for air-traffic management. *Second Aviation, Range, and Aerospace Meteorology Special Symp. on Weather–Air Traffic Management Integration*, Seattle, WA, Amer. Meteor. Soc., 3.2, https://ams.confex.com/ams/91Annual/webprogram/Paper185659.html.

——, and Coauthors, 2013: Data assimilation and model updates in the 2013 Rapid Refresh (RAP) and High-Resolution Rapid Refresh (HRRR) analysis and forecast systems. *NCEP/EMC Meeting*, Washington, DC, NCEP/EMC/Model Evaluation Group, http://ruc.noaa.gov/pdf/NCEP_HRRR_RAPv2_6jun2013-Benj-noglob.pdf.

——, and Coauthors, 2016: A North American hourly assimilation and model forecast cycle: The Rapid Refresh. *Mon. Wea. Rev.*, **144**, 1669–1694, https://doi.org/10.1175/MWR-D-15-0242.1.

Berenguer, M., D. Sempere-Torres, C. Corral, and R. Sanchez-Diezma, 2006: A fuzzy logic technique for identifying nonprecipitating echoes in radar scans. *J. Atmos. Oceanic Technol.*, **23**, 1157–1180, https://doi.org/10.1175/JTECH1914.1.

Brandes, E. A., and K. Ikeda, 2004: Freezing-level estimation with polarimetric radar. *J. Appl. Meteor.*, **43**, 1541–1553, https://doi.org/10.1175/JAM2155.1.

Chandrasekar, V., R. Keränen, S. Lim, and D. Moisseev, 2013: Recent advances in classification of observations from dual polarization weather radars. *Atmos. Res.*, **119**, 97–111, https://doi.org/10.1016/j.atmosres.2011.08.014.

Cheong, B. L., R. Palmer, and S. Torres, 2011: Automatic wind turbine identification using level-II data. *IEEE Radar Conf.*, Kansas, MO, IEEE, 271–275, https://doi.org/10.1109/RADAR.2011.5960542.

Doviak, R. J., and D. S. Zrnić, 1993: *Doppler Radar and Weather Observations*. Academic Press, 562 pp.

Fabry, F., and I. Zawadzki, 1995: Long-term radar observations of the melting layer of precipitation and their interpretation. *J. Atmos. Sci.*, **52**, 838–851, https://doi.org/10.1175/1520-0469(1995)052<0838:LTROOT>2.0.CO;2.

Giangrande, S. E., J. M. Krause, and A. V. Ryzhkov, 2008: Automatic designation of the melting layer with a polarimetric prototype of the WSR-88D radar. *J. Appl. Meteor. Climatol.*, **47**, 1354–1364, https://doi.org/10.1175/2007JAMC1634.1.

Gourley, J. J., and C. M. Calvert, 2003: Automated detection of the bright band using WSR-88D data. *Wea. Forecasting*, **18**, 585–599, https://doi.org/10.1175/1520-0434(2003)018<0585:ADOTBB>2.0.CO;2.

——, P. Tabary, and J. P. Chatelet, 2007: A fuzzy logic algorithm for the separation of precipitating from nonprecipitating echoes using polarimetric radar observations. *J. Atmos. Oceanic Technol.*, **24**, 1439–1451, https://doi.org/10.1175/JTECH2035.1.

Hood, K., S. Torres, and R. Palmer, 2010: Automatic detection of wind turbine clutter for weather radars. *J. Atmos. Oceanic Technol.*, **27**, 1868–1880, https://doi.org/10.1175/2010JTECHA1437.1.

Isom, B. M., and Coauthors, 2009: Detailed observations of wind turbine clutter with scanning weather radars. *J. Atmos. Oceanic Technol.*, **26**, 894–910, https://doi.org/10.1175/2008JTECHA1136.1.

Krause, J. M., 2016: A simple algorithm to discriminate between meteorological and nonmeteorological radar echoes. *J. Atmos. Oceanic Technol.*, **33**, 1875–1885, https://doi.org/10.1175/JTECH-D-15-0239.1.

Kumjian, M. R., 2013a: Principles and applications of dual-polarization weather radar. Part I: Description of the polarimetric radar variables. *J. Oper. Meteor.*, **1**, 226–242, https://doi.org/10.15191/nwajom.2013.0119.

——, 2013b: Principles and applications of dual-polarization weather radar. Part II: Warm- and cold-season applications. *J. Oper. Meteor.*, **1**, 243–264, https://doi.org/10.15191/nwajom.2013.0120.

Lakshmanan, V., J. Zhang, K. Hondl, and C. Langston, 2012: A statistical approach to mitigating persistent clutter in radar reflectivity data. *IEEE J. Sel. Top. Appl. Earth Obs. Remote Sens.*, **5**, 652–662, https://doi.org/10.1109/JSTARS.2011.2181828.

——, C. Karstens, J. Krause, and L. Tang, 2014: Quality control of weather radar data using polarimetric variables. *J. Atmos. Oceanic Technol.*, **31**, 1234–1249, https://doi.org/10.1175/JTECH-D-13-00073.1.

Liu, H., and V. Chandrasekar, 2000: Classification of hydrometeors based on polarimetric radar measurements: Development of fuzzy logic and neuro-fuzzy system, and in situ verification. *J. Atmos. Oceanic Technol.*, **17**, 140–164, https://doi.org/10.1175/1520-0426(2000)017<0140:COHBOP>2.0.CO;2.

Melnikov, V. M., and D. S. Zrnić, 2007: Autocorrelation and cross-correlation estimators of polarimetric variables. *J. Atmos. Oceanic Technol.*, **24**, 1337–1350, https://doi.org/10.1175/JTECH2054.1.

Nai, F., R. Palmer, and S. Torres, 2011: Wind turbine clutter mitigation using range-Doppler domain signal processing method. *27th Conf. on Interactive Information and Processing Systems*, Seattle, WA, Amer. Meteor. Soc., 9.4, https://ams.confex.com/ams/91Annual/webprogram/Paper183727.html.

Norin, L., and G. Haase, 2012: Doppler weather radars and wind turbines. *Doppler Radar Observations—Weather Radar, Wind Profiler, Ionospheric Radar, and Other Advanced Applications*, J. Bech and J. L. Chau, Eds., InTech, 333–354.

Park, H. S., A. V. Ryzhkov, D. S. Zrnić, and K.-E. Kim, 2009: The hydrometeor classification algorithm for the polarimetric WSR-88D: Description and application to an MCS. *Wea. Forecasting*, **24**, 730–748, https://doi.org/10.1175/2008WAF2222205.1.

Ryzhkov, A. V., and D. S. Zrnić, 2019: *Radar Polarimetry for Weather Observations*. Springer Atmospheric Sciences, Springer International Publishing, 486 pp.

Smith, T. M., and Coauthors, 2016: Multi-Radar Multi-Sensor (MRMS) severe weather and aviation products: Initial operating capabilities. *Bull. Amer. Meteor. Soc.*, **97**, 1617–1630, https://doi.org/10.1175/BAMS-D-14-00173.1.

Steiner, M., and J. A. Smith, 2002: Use of three-dimensional reflectivity structure for automated detection and removal of nonprecipitating echoes in radar data. *J. Atmos. Oceanic Technol.*, **19**, 673–686, https://doi.org/10.1175/1520-0426(2002)019<0673:UOTDRS>2.0.CO;2.

Tabary, P., A. Le Henaff, G. Vulpiani, J. Parent-du-Chatelet, and J. J. Gourley, 2006: Melting layer characterization and identification with a C-band dual-polarization radar: A long-term analysis. *Fourth European Conf. on Radar in Meteorology and Hydrology*, Barcelona, Spain, Servei Meteorologic de Catalunya, 17–20.

Tang, L., J. Zhang, C. Langston, J. Krause, K. W. Howard, and V. Lakshmanan, 2014: A physically based precipitation–nonprecipitation radar echo classifier using polarimetric and

environmental data in a real-time national system. *Wea. Forecasting*, **29**, 1106–1119, https://doi.org/10.1175/WAF-D-13-00072.1.

——, ——, ——, and K. Cooper, 2016: Canadian radar quality control in Multi-Radar-Multi-Sensor system. *Fifth Aviation, Range and Aerospace Meteorology Special Symp.*, New Orleans, LA, Amer. Meteor. Soc., 835, https://ams.confex.com/ams/96Annual/webprogram/Paper282745.html.

Vogt, R. J., J. R. Reed, T. Crum, J. T. Snow, R. Palmer, B. Isom, and D. W. Burgess, 2007: Impacts of wind farms on WSR-88D operations and policy considerations. *23rd Int. Conf. on Interactive Information Processing Systems for Meteorology, Oceanography, and Hydrology*, San Antonio, TX, Amer. Meteor. Soc., 5B.7, https://ams.confex.com/ams/87ANNUAL/techprogram/paper_120352.htm.

——, T. D. Crum, W. Greenwood, E. J. Ciardi, and R. G. Guenther, 2011: New criteria for evaluating wind turbine impacts on NEXRAD radars. *American Wind Energy Association Conf. and Exhibition*, Anaheim, CA, American Wind Energy Association.

Walpole, R. E., R. H. Myers, S. L. Myers, and K. E. Ye, 2016: *Probability and Statistics for Engineers and Scientists*. 9th ed. Pearson, 816 pp.

White, A. B., D. J. Gottas, E. T. Strem, F. M. Ralph, and P. J. Neiman, 2002: An automated brightband height detection algorithm for use with Doppler radar spectral moment. *J. Atmos. Oceanic Technol.*, **19**, 687–697, https://doi.org/10.1175/1520-0426(2002)019<0687:AABHDA>2.0.CO;2.

Wolfensberger, D., D. Scipion, and A. Berne, 2016: Detection and characterization of the melting layer based on polarimetric radar scans. *Quart. J. Roy. Meteor. Soc.*, **142**, 108–124, https://doi.org/10.1002/qj.2672.

Zhang, J., and Y. Qi, 2010: A real time algorithm for the correction of brightband effects in radar-derived QPE. *J. Hydrometeor.*, **11**, 1157–1171, https://doi.org/10.1175/2010JHM1201.1.

——, S. Wang, and B. Clarke, 2004: WSR-88D reflectivity quality control using horizontal and vertical reflectivity structure. *11th Conf. on Aviation, Aviation, Range and Aerospace Meteorology Special Symp.*, Hyannis, MA, Amer. Meteor. Soc., P5.4, http://ams.confex.com/ams/11aram22sls/techprogram/programexpanded_229.htm.

——, and Coauthors, 2016: Multi-Radar Multi-Sensor (MRMS) quantitative precipitation estimation: Initial operating capabilities. *Bull. Amer. Meteor. Soc.*, **97**, 621–638, https://doi.org/10.1175/BAMS-D-14-00174.1.

Zrnić, D. S., and A. V. Ryzhkov, 1999: Polarimetry for weather surveillance radars. *Bull. Amer. Meteor. Soc.*, **80**, 389–406, https://doi.org/10.1175/1520-0477(1999)080<0389:PFWSR>2.0.CO;2.